Published in final edited form as:
J Control Release. 2011 February 10; 149(3): 314–322. doi:10.1016/j.jconrel.2010.10.030.

Enhanced noscapine delivery using uPAR-targeted optical-MR imaging trackable nanoparticles for prostate cancer therapy

Mohamed O. Abdalla[1,2], **Prasanthi Karna**[1], **Hari Krishna Sajja**[1], **Hui Mao**[3], **Clayton Yates**[2], **Timothy Turner**[2], and **Ritu Aneja**[1,*]

[1]Department of Biology, Georgia State University, Atlanta, GA 30303

[2]Department of Biology and Center for Cancer Research, Tuskegee, AL 36088

[3]Department of Radiology, Emory University School of Medicine, Atlanta, GA 30322

Abstract

The tubulin-binding anticancer activity of noscapine, an orally-available plant-derived anti-tussive alkaloid, has been recently identified. Noscapine inhibits tumor growth in nude mice bearing human xenografts of hematopoietic, breast, lung, ovarian, brain and prostate origin. Despite its non-toxic attributes, significant elimination of the disease has not been achieved, perhaps since the bioavailability of noscapine to tumors saturates at an oral dose of 300 mg/kg body weight. To enable the selective and specific delivery of noscapine to prostate cancer cells, we have engineered a multifunctional nanoscale delivery vehicle which takes advantage of urokinase plasminogen activator receptor (uPAR) overexpression in prostate cancer compared to normal prostate epithelia and can be tracked by magnetic resonance imaging (MRI) and near-infrared (NIR) imaging. Specifically, we employed the human-type 135 amino-acid amino-terminal fragment (hATF) of urokinase plasminogen activator (uPA), a high-affinity natural ligand for uPAR. Noscapine (Nos) was efficiently adsorbed onto the amphiphilic polymer coating of uPAR-targeted nanoparticles (NPs). Nos-loaded NPs were uniformly compact-sized, stable at physiological pH and efficiently released the drug at pH 4 to 5 within a span of 4 h. Our results demonstrate that these uPAR-targeted NPs were capable of binding to the receptor and were internalized by PC-3 cells. uPAR-targeted Nos-loaded NPs enhanced intracellular noscapine accumulation as evident by the ~6-fold stronger inhibitory effect on PC-3 growth compared to free noscapine. In addition, Nos-loaded iron oxide NPs maintained their T2 MRI contrast effect upon internalization into tumor cells owing to their significant susceptibility effect in cells. Thus, our data provide compelling evidence that these optically- and magnetic resonance imaging (MRI)- trackable uPAR-targeted NPs may offer a great potential for image-directed targeted delivery of noscapine for the management of prostate cancer.

Keywords

Prostate; Noscapine; Nanoparticles; uPAR; MRI

*Address for correspondence: Ritu Aneja, Department of Biology, Georgia State University, Atlanta, GA 30303; raneja@gsu.edu.

1. Introduction

Despite advances in diagnosis and treatment, prostate cancer continues to be one of the deadliest cancers and ranks the second most frequent cause of cancer-related deaths in males in the United States [1]. Although current chemotherapeutics including docetaxel have shown promise for the treatment of hormone-refractory prostate cancer, toxicity has been a serious limitation associated with systemic chemotherapy [2]. Thus, novel strategies including targeted therapies are gaining importance and are being intensively investigated [3–4].

Multifunctional iron oxide nanoparticles (IO NPs) have recently emerged as attractive candidates for cancer chemotherapeutic approaches that obviate toxicity issues and display improved tumor targeting [3, 5–9]. A key component of multifunctional NPs is the tumor-targeting moiety that guides them to cancer-specific receptors with high-affinity and specificity [10–12]. A specific prostate cancer target and a useful biomarker, the urokinase-type plasminogen activator (uPA) and its receptor (uPAR) are selectively overexpressed at high levels in invasive prostate cancer, sparing the normal prostate epithelia[13]. Owing to the differential expression of uPA and uPAR in cancer tissues relative to normal tissues, they are being employed for potential prognostic and/or therapeutic applications [14–16]. The amino terminal fragment (ATF) of uPA, which consists of 135 amino acids is, in particular, a desirable homing moiety as it contains all the determinants required for uPAR binding [17–19]. Recently, Yang et al. reported murine ATF as a targeting moiety to guide iron oxide NPs for *in vivo* imaging of breast cancer [20]. Since ATF is a remarkable targeting moiety for tumor cells, it can be advantageously employed as a therapeutic-vehicle to steer ‘drug-loaded’ NPs selectively to tumor sites.

Noscapine, an antitussive agent, has been discovered as a tubulin-binding anticancer drug, and is in Phase I/II clinical trials for the treatment of multiple myeloma. Noscapine does not change the steady state monomer/polymer ratio of tubulin [21–23]. Thus, noscapine does not cause any hemo-, immuno- and neuronal toxicity [21]. This is a unique-edge over currently-available antimicrotubule drugs that either overpolymerize microtubules (*taxanes*) or depolymerize them (*vincas*) and hence cause various toxicities such as leucocytopenias, and peripheral neuropathies [24–27]. Extensive studies have reported the potential usefulness of noscapine in the therapy of lymphomas, melanoma, prostate and lung cancers [28–31]. The pharmacokinetics of noscapine has also been reported [32] showing that the orally administered drug peaks within 2–3 h and is not detectable after 6 h, indicating the short circulation time of noscapine in the system [33–34].

Although noscapine has been shown to significantly inhibit tumor growth in preclinical mice models [21–22, 31, 35], near-complete tumor elimination has not been achieved even after increasing the dosage to 450 mg/kg. This is perhaps due to its shorter circulation time as well as to the possible saturation of drug uptake by tumor cells. In this study, we present the design, preparation, optimization and characterization of multifunctional nanoparticles that significantly enhanced noscapine uptake by making noscapine ‘targetable’ to cancer cells. We report the development of a multifunctional nanoparticle delivery vehicle which can be tracked by magnetic resonance imaging (MRI) and near infrared (NIR) imaging and takes advantage of uPAR overexpression to selectively and preferentially deliver noscapine in prostate cancer cells. This novel delivery approach allows for enhanced intracellular noscapine accumulation to selectively cause significant growth inhibition and cell death in prostate cancer cells.

2. Materials and Methods

2.1. Chemicals and reagents

Polymer coated IO NPs with carboxylic acid reactive groups, and the conjugation kit were from Ocean Nanotech (Springdale, AR). Noscapine hydrochloride, Isopropyl-β-D-thiogalactopyranoside (IPTG), *N*-hydroxysulfosuccinimide (Sulfo-NHS), 1-ethyl-3-[3-dimethylaminopropyl]carbodiimide (EDAC), tris(2-carboxyethyl)-phosphine (TCEP) were from Sigma (St. Louis, MO). Cy5.5 monomaleimide was from GE Healthcare (Piscataway, NJ). The peptide, human-type ATF (hATF) of the uPA, was produced and purified.

2.2. Cancer cell lines

Human prostate carcinoma (LNCaP, DU-145 and PC-3) cells were cultured in RPMI-1640 supplemented with 10% FBS. Human prostate carcinoma, RC-77T/E, and normal prostate epithelial cells, RC-77N/E, were maintained in Gibco Keratinocyte-SFM medium (Invitrogen, Carlsbad, CA) supplemented with EGF (human recombinant) and bovine pituitary extract. Human embryonic kidney cells (HEK293) were cultured in DMEM.

2.3. Preparation and characterization of hATF-Cy5.5-IO-Nos NPs

2.3.1 Production of recombinant hATF—A cDNA fragment encoding the first 135 amino acids of human uPA was isolated by PCR amplification and cloned into pET-20(b) expression vector. Initial plasmid cloning and sequence verification was carried out in *E. coli* Top 10 F′ cells. After the plasmid was verified to contain the correct hATF sequence, the plasmid was purified and transformed into *E. coli* BL-21 for peptide expression using IPTG induction and purification under native conditions using FPLC (Amersham BioSciences).

2.3.2. hATF-Cy5.5 conjugation—Cy5.5 monomaleimide was used to conjugate fluorescent Cy5.5 dye with hATF at cysteine residues using the manufacturer's protocol (GE Healthcare, Piscataway, NJ). Free dye molecules were separated using Nanosep 3K centrifugation column (Pall Corp, Ann Arbor, MI). The prepared hATF-Cy5.5 conjugate was PBS washed and used immediately or stored at 4°C.

2.3.3. Conjugation of hATF or hATF-Cy5.5 complex to IO NPs—We used ~10 nm core size IO NPs for this study. The core size and hydrodynamic size of IO NPs were measured using transmission electron microscopy (TEM) and light scattering scan, respectively. The particles were coated with amphiphilic triblock polymers which stabilize IO NPs in water and provide reactive carboxyl groups on the particle surface for bioconjugation. hATF peptides were conjugated to the surface of IO NPs via cross -linking of carboxyl groups to amino side groups on hATF peptides. Briefly, polymer-coated IO NPs were activated with EDAC and sulfo-NHS for 15 min in 20 mM borate buffer (pH 5.0). The activated IO NPs were purified using Nanosep 100k columns and reacted with hATF or hATF-Cy5.5 complex (ratio of 1:10) in 10 mM borate buffer (pH 8.5) for 2h at room temperature and then overnight at 4°C to generate hATF-IO or hATF-Cy5.5-IO NPs. The resulting Cy5.5-hATF-IO or hATF-IO were separated from the reaction buffer using Nanosep 100K column. The conjugates were purified by washing with PBS buffer followed by resuspension in sterile distilled water, and stored at 4°C.

2.3.4. Particle size and zeta potential measurements—To determine the size of the non-targeted IO NPs (NT-IO NPs), hATF-Cy5.5-IO and hATF-Cy5.5-IO-Nos, TEM was performed using negative staining method (TEM LEO906E, Oberkochen, Germany). The size of NPs was determined from TEM images. The mean hydrodynamic particle size and zeta potential of the various NPs were determined using dynamic laser scattering (Zetasizer-

II, Malvern Instruments, Worcestershire, UK). All measurements were made at a scattering angle of 90° at 25°C.

2.3.5. Encapsulation of Noscapine (Nos) onto hATF-Cy5.5-IO NPs—An aqueous solution of noscapine (1 mg/mL) was added to NT-IO or hATF-Cy5.5-IO NPs at a ratio of 1 mg drug to 3 mg of iron (Fe) and the mixture was rotated at RT for 4h and then at 4°C overnight. After filtration of NPs through the 100K Nanosep column, the free drug was analyzed by HPLC (Agilent 1100). Encapsulation efficiency of noscapine was calculated as the mass ratio of the amount of drug entrapped in nanoparticles to the initial amount used in drug loading. The number of Nos molecules encapsulated in an IO nanoparticle was derived by dividing the total number of Nos molecules by the total number of IO NPs in each sample. The total number of IO NPs was determined by measuring the optical density (OD) at 500 nm for Fe concentration. The concentration of Fe was then used to calculate the number of IO NPs using a standard formula.

2.3.6. pH-dependent drug release—The pH-dependent drug release was determined by incubating drug containing NPs in solutions of different pH (4, 5, 6, or 7) and measuring Nos concentration in the flow-through by HPLC. The free drug molecules in the buffer were then separated from the NT-IO and hATF-IO-Cy5.5NPs using 100K Nanosep column. The amount of free Nos was calculated from a standard curve of drug concentration and HPLC signal intensity.

2.4. hATF-mediated binding efficacy of NPs to PC-3 Cells

2.4.1. siRNA knockdown of uPAR expression—Human uPAR siRNA (Santa Cruz, CA) is a pool of three target-specific 20–25 nt siRNAs designed to knockdown uPAR gene expression. Cells were transfected with the pool of three target-specific 20–25 nt siRNAs to human uPAR according to the manufacturer's protocol. A scrambled siRNA sequence was used in parallel as a control. After 48 h, uPAR levels decreased by ~80–90% as confirmed by western blotting.

2.4.2 Western blotting—LNCaP, DU-145, PC-3, RC-77T/E, control or uPAR siRNA transfected PC-3 cell lysates were subjected to immunoblotting. Membranes were probed with rabbit anti-uPAR antibody (American Diagnostica, Greenwich, CT) followed by HRP-conjugated secondary antibody (Santa Cruz, CA). uPAR was detected by chemiluminescence method.

2.4.3. Prussian blue staining—Prussian blue staining was used to confirm presence of iron in cells treated with IO NPs. Control or uPAR siRNA transfected PC-3 cells or untransfected LNCaP cells were incubated with 30 pmole/mL of NT-IO or hATF-Cy5.5-IO NPs for 4h followed by staining with Prussian blue (1:1 mixture of 5% potassium ferrocyanide and 5% HCl) for 4h at RT. Bright field images were obtained and blue-stained cells were quantified and represented as percentage of positive cells compared to total number of cells.

2.4.4. In vitro near-infrared optical imaging—PC-3 cells cultured in 12-well plates were incubated with various concentrations (20, 30, 40 pmole/mL) of hATF-Cy5.5-IO NPs for 4h at 37°C. Control samples were incubated with equal amounts of hATF-IO NPs at similar conditions. Cells were then washed, fixed and imaged using a Perkin-Elmer Ultraview ERS microscope with an excitation wavelength of 650 nm and an emission of 680 nm.

2.4.5. *In vitro* MRI Scan—PC-3, LNCaP and HEK293 cells were incubated with 40 pmole/mL of hATF-Cy5.5-IO or NT-IO NPs for 2h at 37°C. Cells were washed, trypsinized, collected and then embedded in 1% agarose in 1.5 mL eppendorf tubes. Samples were scanned using a 3-T MRI scanner (Siemens Healthcare) using T1-weighted gradient echo and multi-echo T2-weighted fast-spin echo imaging sequences. T2 values of each sample were calculated from obtained multi-echo (TE_i, i=20, range from 10–200 ms, interval=10 ms). Transverse relaxation times, T2, of each sample were calculated by fitting decay curve on a pixel-by-pixel basis using the nonlinear mono-exponential algorithm of $M_i = M_0 * \exp(-TE_i/T_2)$, in which M_o is the MRI signal intensity at TE of 0 and M_i is the MRI signal intensity at a selected TE.

2.6. Cytotoxicity assay

RC-77NE, PC-3 or uPAR siRNA transfected cells were treated with serum-free medium containing NT-IO-Nos or hATF-Cy5.5-IO-Nos NPs, or free Nos (10 μM). Control groups were treated with NT-IO or hATF-IO-NPs without Nos that had equal amounts of IO as test samples. Cells were incubated for 4h, followed by serum addition to the medium for an additional 48h. Percentage of tumor cell death was determined by crystal violet assay. The optical density was read at 590 nm using a microplate reader (SpectroMax, Molecular Devices). Absorbance values were normalized to control values to obtain the percentage of viable cells.

2.7. Statistical analyses

Data are presented as mean ± SEM of at least 3 separate experiments performed in triplicate. $P<0.05$ was considered statistically significant.

3. Results and Discussion

3.1. Design, preparation, characterization and optimization of multifunctional NPs

We have designed, developed and optimized ‘multifunctional’ NPs using a recombinant peptide hATF of uPA conjugated to magnetic IO NPs. The NIR imaging dye Cy5.5 was conjugated to cysteine residues of hATF. Subsequently, using amino groups of amino terminus and those of lysine residues from hATF, the hATF-Cy5.5 bi-conjugate was coupled with carboxyl ends offered by the amphiphilic polymer coating on IO core to form tri-conjugate hATF-Cy5.5-IO NPs. Finally, noscapine was loaded on the tri-conjugate molecule by physical adsorption onto the IO NP polymer coating (Scheme 1).

3.1.1. Size characterization of various conjugates

3.1.1.1. Transmission electron microscopy (TEM): Effective drug delivery to tumor tissue requires appropriately sized NPs that can stay in the blood-stream for requisite time to selectively release their payload at the tumor site [36]. Since elevated levels of vascular permeability characterize most solid tumors, it is pertinent for NPs to possess a compact size to steer through immature and leaky tumor vessels and proficiently enter tumor mass [37]. Thus, ideally NPs should be large enough (>10 nm) to prevent their rapid leakage into blood capillaries but small enough (<100 nm) to escape capture by macrophages that are lodged in the reticuloendothelial system [36, 38]. We first examined the size of NT- IO NPs using TEM to assess increase in their size at varying stages of each conjugation step. Fig. 1 (left) presents TEM image of NT-IO NPs, which confirmed the uniformity of the core IO NPs with an average diameter of 11.2 ± 2.5 nm. Next, we attempted to visualize the size of the polymer coating surrounding the IO core. To this end, we stained NT-IO NPs using phosphotungstic acid to contrast the thin polymer layer with an optically opaque fluid. Fig. 2 (middle) shows negatively stained NT-IO NPs that determined the polymer coating to be at

an average of 4.2 nm making the overall size of these particles to be 15 ± 3.1 nm. It was not possible to determine the exact increase in size of the polymer coated IO NPs after conjugation of hATF-Cy5.5 and drug loading (Fig. 1, right).

3.1.1.2. Dynamic light scattering (DLS): To measure size of the prepared NP conjugates, we used DLS to measure size of NP conjugates that provides size distribution of NPs in addition to their hydrodynamic size. The size distribution reveals formation of any aggregates upon conjugation of protein and drug loading. Table 1 presents hydrodynamic size data of NT-IO, hATF-Cy5.5-IO, hATF-Cy5.5-IO-Nos NPs. NPs retained a narrow size distribution after conjugation of peptide-dye and drug loading. As expected, the size of NT-IO NPs (21.36 ± 1.6 nm) increased upon conjugation of hATF-Cy5.5 (35.21 ± 3.7 nm) to their outer surface while it remained relatively constant upon drug loading (35.62 ± 4.1 nm). In general, overall size of the nanoscale drug delivery vehicle was uniform and within the desired size range of 10–100 nm for optimal drug delivery [36, 38].

3.1.2. Surface charges of NPs at varying stages of build-up—The surface charge of NPs determines their circulation time in blood stream and is a measure of NP stability in aqueous solution and their interaction with the cell membrane [39]. Table 1 collates zeta potential measurements. The NT-IO NPs had a negative charge of −52.41 ± 3.1 mV on the surface, which is due to carboxylic groups of polymer coating. This value correlated with the value (−51.41 mV) provided in the Certificate of Analysis of NT-IO NPs from the manufacturer. Conjugation of hATF-Cy5.5 to some of the carboxylic ends resulted in a decrease of surface charge of NPs to −33.4 ± 5.61 mV for hATF-Cy5.5-IO NPs. The loading of hydrophobic Nos on the hATF-Cy5.5-IO NPs further decreased the surface charge to −21.6 ± 3.3 mV. Despite surface charge decrease of hATF-Cy5.5-IO-Nos NPs, they were well-dispersed in sterile water with no observable precipitation for a few months. The stability of drug-loaded NPs in aqueous media is crucial for potential biomedical applications as no vehicle solution is needed to inject them. Moreover, surface charge data reflect that hydrophilicity of NPs did not decrease which in clinical settings may prevent their opsonization by plasma proteins and elongate their blood circulation time.

3.1.3 Efficiency of noscapine loading—Incorporation of sufficient drug amounts onto NPs is vital for effective therapy. Based on drug properties, it can either be covalently conjugated to the polymer coating of NPs or can be physically adsorbed onto the polymer coating [12, 40]. A downside of covalent linking is that it may limit the amount of drug molecules conjugated to each NP as well as present a low efficiency of drug release upon cell entry. Physical adsorption of drug molecules onto NPs, on the contrary, may ferry more drug molecules into cells and release the drug efficiently. Thus, we next investigated the efficiency of noscapine encapsulation in the prepared uPAR-targeted NPs. Using a ratio of 1 mg drug to 3 mg IO, we were able to encapsulate 98.7% of Nos onto the NT-IO NPs (Table 2) as determined by HPLC analysis. This high drug encapsulation efficiency may perhaps be due to a favorable interaction between the hydrophobic noscapine molecules and the hydrophobic segment of the amphiphilic polymer coating of NPs. We observed that there was a 10% decrease in efficiency of drug encapsulation when Nos was loaded after conjugation of hATF-Cy5.5 to the surface of IO NPs. The decrease in drug encapsulation was perhaps attributed to steric hindrance to the drug molecules caused by the space occupied by the hATF-Cy5.5 conjugates on the surface of IO NPs [41]. Table 2 also shows the number of Nos molecules adsorbed per IO NPs in NT IO NPs as well as in NPs with the conjugated targeting moiety-dye (hATF-Cy5.5). There was a ~24% percent reduction in the number of Nos molecules adsorbed on the surface of NT-IO and hATF-Cy5.5-IO NPs. The difference in percent drug encapsulation and percent decrease in the number of adsorbed

Nos molecules per IO NP may perhaps be due to uneven drug encapsulation in a given sample.

3.1.4. pH-dependent drug release characteristics from multifunctional NPs—It is recognizable that the efficiency of any drug delivery vehicle is best evaluated by its ability to release the 'payload' drug into cells and not systemically in the patient's circulation system. To simulate physiological conditions, we examined the amount of Nos that can be released from the NPs at pH 7. Slightly acidic pH conditions simulated the environment of tumor interstitium, while more acidic pH was more representative of the pH in intracellular vesicles such as endosomes and lysosomes. Fig. 2A shows overlays of HPLC chromatograms to depict the amount of Nos detected in the supernatant of hATF-Cy5.5-IO-Nos NPs at various pHs. At pH 7, no peak was detected for Nos indicating that the drug was not released due to its strong adsorption to the polymer coating on the IO NPs (Fig. 2B). However, when the pH was lowered, the amount of detected Nos increased with the increase in the acidity of the medium. The area under the peak was used to calculate the percentage of drug release from the NT-IO-Nos or hATF-Cy5.5-IO-Nos NPs (Fig. 2B). While no drug was detected at pH 7, the NPs released about ~25–30% of their drug payload at pH 6. At pH 5, the percentage of drug released from NPs increased to ~60%. At pH 4, over ~80% of drug molecules were efficiently released from NPs. These results indicated strong adsorption of drug onto the IO NP surface, thus facilitating drugs release at acidic pH. Enhancement of drug release may be due to the onset of polymer degradation at lower pH or the breakage of hydrophobic interactions between polymer and drug molecules. Another plausible explanation for enhanced drug release at lower pH exists based upon hydrogen bonding. Since the lower benzofuranone ring of noscapine has electronegative oxygen atoms (particularly the 'two oxygens' in the lactone ring of the molecule) that can participate in hydrogen bonding, the extent of hydrogen bonding of noscapine would reduce with decrease in pH (protonation) resulting in a pH dependent drug release. In conclusion, these data suggested that the targeted NPs can serve as efficient carriers of drug payload that can be delivered in acidic environments which particularly exist in the hypoxic tumor milieu.

3.2. Binding and internalization efficiency of hATF-targeted NPs

3.2.1. Determination of uPAR expression in various prostate cancer cells—Previous studies have shown that PC-3 cells are highly metastatic, whereas DU145 and LNCaP cells are moderately and poorly metastatic, respectively [15, 42–43]. Because uPAR is important for tumor invasion and metastasis, we first compared uPAR expression level in various prostate cancer cell lines with different metastatic potentials. As shown in Fig. 3A, uPAR levels corresponded well with the metastatic potential of cells. uPAR expression was significantly higher in PC-3 and DU145 cells compared to LNCaP and RC-77T/E cells (Fig. 3A). More importantly, the normal prostate cells, RC77N/E, showed very low levels of uPAR expression, suggesting that uPAR is selectively overexpressed in cancer cells and almost spares normal cells. Having identified expression levels of uPAR, we next evaluated the uptake efficiency of targeted and non-targeted IO NPs by these cells with varying uPAR expression.

3.2.2. Prussian blue staining—Previous reports show that the binding of ATF to uPAR has species specificity [18]. Thus, to preserve species specificity, we employed human ATF rather than murine ATF as previously reported [18]. The binding of hATF peptide to high uPAR-expressing PC-3 and low uPAR-expressing LNCaP cells was investigated. Subsequent to binding, the consequent internalization was examined by Prussian blue staining that stains iron. Fig. 3B shows bright field images of PC-3 cells treated with NT-IO and hATF-Cy5.5-IO NPs. Low-uPAR expressing LNCaP cells were treated with hATF-Cy5.5-IO NPs. Fig. 3C presents quantitation data of percent blue-stained cells. PC-3 cells

incubated with hATF-Cy5.5-IO NPs showed a high level of iron staining (>80% blue-stained cells) both intra and extracellularly which suggested that targeted NPs were able to bind and be internalized by the uPAR-overexpressing PC-3 cells. PC-3 cells incubated with NT-IO exhibited a very low level of non-specific iron staining. Next, we performed an indirect experiment to demonstrate that the internalization of targeted NPs is mediated by the interaction of hATF with uPAR displayed on PC-3 cells. To this end, we saturated uPAR sites on PC-3 cells by adding an excess of free hATF peptide (1h) prior to addition of targeted NPs. Fig. 3B (bottom left) shows micrographs of uPAR-saturated PC-3 cells that exhibited a much lower iron staining compared to non-saturated PC-3 cells (<20% blue-stained cells). Next, we incubated low uPAR-expressing LNCaP cells with targeted NPs. Fig. 3B (bottom right) shows micrographs of LNCaP cells with insignificant amount of scattered non-specific iron staining (<5% blue-stained cells). These data suggested that high uPAR expression in PC-3 cells facilitated binding and internalization of targeted NPs.

3.2.3. In vitro near-infrared (NIR) optical imaging—We further confirmed the binding and internalization of the targeted multifunctional NPs in PC-3 cells using confocal microscopy by imaging the NIR-dye, Cy5.5 which was conjugated to the hATF peptide. To this end, PC-3 cells were treated with increasing amounts of the hATF-Cy5.5-IO NPs and DIC (differential interference contrast) as well as NIR images were acquired (Fig. 4A, B). Our results showed an increase in the number of Cy5.5-positive cells with increase in concentration of iron oxide in the hATF-Cy5.5-IO NPs (Fig. 4B). Quantitation of Cy5.5-positive cells is shown in Fig. 4B. The percentage of Cy5.5 cells increased from ~45% to ~60% on increasing the dose level from 20 pmol to 30 pmol and peaked to a maximum of ~90% at 40 pmol of iron oxide in the NPs. This data validated the high-affinity binding between hATF guided IO NPs and uPAR displayed on the surface of tumor cells. As a negative control, we treated PC-3 cells with hATF-IO NPs and as expected, there was no NIR signal due to absence of Cy5.5 moiety. The incorporation of Cy5.5 in NPs might offer a simple and sensitive approach to quantify tumor targeting and to monitor distribution of NPs in small animal models. Furthermore, the multifunctional hATF-Cy5.5-IO NPs offer the prospect to image both primary and metastatic tumor lesions with hATF-guided NPs that target high-uPAR expressing prostate cancer at their invasive sites.

3.2.4. In vitro magnetic resonance imaging (MRI)—Multifunctional nanoparticles can serve to simultaneously deliver anticancer drugs and allow tumor imaging and are being increasingly investigated for their improved therapeutic efficacy and lower toxicity. Superparamagnetic IO NPs are widely used as contrast agents in MRI because of their negative enhancement effect on T2-weighted sequences. Our multifunctional NPs included the iron oxide core which typically induces reduction of transverse relaxation time and T2-weighted contrast change. The signal drops in MRI allow for tracking the targeted drug delivery using clinically capable MRI systems. MRI scans of untreated as well as treated PC-3 cells with NT-IO and hATF-Cy5.5-IO NPs are shown in Fig. 5A. LNCaP and HEK293 treated with hATF-Cy5.5-IO NPs were used as controls. The MR images demonstrated significant target specificity. A pronounced reduction of T2 values was detected in PC-3 cells treated with the hATF-Cy5.5-IO NPs. This indicated that high amounts of IO are bound to high uPAR-expressing PC-3 cells. On the other hand, both LNCaP and HEK293 cells incubated with hATF-Cy5.5-IO NPs did not exhibit the MRI signal drop with T2 weighted contrast and reduction of T2 values. These results corroborated our Prussian blue staining and NIR optical imaging data emphasizing that uPAR expression was essential for successful binding and internalization of the targeted NPs by PC-3 cells. Fig. 5B presents MRI signal differences of different samples in T2-weighted images which correlated well with the reduction in the T2 values of different samples. We found that PC-3 cells treated with targeted hATF-Cy5.5-IO NPs appeared dark in the T2-weighted MR image due to the

presence of high level of hATF-IONPs (Fig. 5B). On the contrary, untreated PC-3, NT-IO NPs treated PC-3, and hATF-Cy5.5-IO NPs treated LNCaP and HEK293 cells remained bright and indistinguishable due to the absence of iron.

3.3. uPAR-targeted noscapine-loaded IO NPs exert a robust cytotoxic effect

To evaluate the selective advantage of targeted NPs to enhance noscapine delivery, we examined the cytotoxic effect of Nos-loaded targeted or non-targeted IO NPs on PC-3 cells. The hATF-Cy5.5-IO-Nos NPs caused ~60% cell death compared to NT-IO-Nos. However, free Nos at the same concentration (10 μM) did not show pronounced cell death. Next, we measured concentration of free noscapine required to achieve ~60% cell death. To this end, we conducted a dose-dependent experiment by treating PC-3 cells with 10–100 μM concentration of free Nos. As shown in Fig 6B, the equivalent dose of free Nos to achieve ~60% cell death was 60 μM. Thus, the uPAR-targeted NPs caused ~6-fold enhancement in cell death compared to the free drug. This enhancement may be ascribed to the efficient intracellular drug delivery by the targeted NPs. Next, we used human uPAR siRNA to knockdown uPAR gene expression in PC-3 cells. The efficiency of gene knockdown was confirmed by immunoblot analysis as shown in Fig 6C. The normal prostate epithelial cells, RC77-N/E, did not express a detectable amount of this protein. Next, we determined the cytotoxicity of hATF-Cy5.5-IO Nos NPs on PC-3 and normal prostate RC-77N/E cells with silenced uPAR expression. Fig 6D showed that ~20% cell death was observed in PC-3 cells with silenced uPAR and no almost cell death was seen in RC77-N/E. These experiments confirmed the targeted delivery of noscapine via the uPA-uPAR system.

4. Conclusion

We have demonstrated the design, development, characterization and optimization of noscapine-loaded uPAR-targeted iron oxide NPs for efficient delivery of the noscapine into prostate cancer cells. Guided by the highly specific and selective ATF of the uPA receptor, the NPs bind to uPA receptor and were internalized by PC-3 cells. The targeted release of noscapine from NPs resulted in a ~6-fold higher drug efficacy compared to free drug. In conclusion, these multifunctional NPs offer NIR-MRI dual imaging functionality provided by the Cy5.5 (NIR) and the iron oxide core (MRI) in addition to targeted drug delivery.

Acknowledgments

This work was supported by grants to RA from NCI/NIH, DoD and GRA. TT and CY acknowledge grant support from NCI/NIH and NIH/RCMI.

References

1. Jemal A, Siegel R, Ward E, Hao Y, Xu J, Thun MJ. Cancer Statistics, 2009. CA Cancer J Clin. 2009; 59:225–249. [PubMed: 19474385]
2. Petrylak DP. The treatment of hormone-refractory prostate cancer: docetaxel and beyond. Rev Urol. 2006; 8(Suppl 2):S48–55. [PubMed: 17021642]
3. Sajja HK, East MP, Mao H, Wang YA, Nie S, Yang L. Development of multifunctional nanoparticles for targeted drug delivery and noninvasive imaging of therapeutic effect. Curr Drug Discov Technol. 2009; 6:43–51. [PubMed: 19275541]
4. Kim K, Kim JH, Park H, Kim YS, Park K, Nam H, Lee S, Park JH, Park RW, Kim IS, Choi K, Kim SY, Kwon IC. Tumor-homing multifunctional nanoparticles for cancer theragnosis: Simultaneous diagnosis, drug delivery, and therapeutic monitoring. J Control Release. 2010; 146:219–227. [PubMed: 20403397]
5. Xie J, Huang J, Li X, Sun S, Chen X. Iron oxide nanoparticle platform for biomedical applications. Curr Med Chem. 2009; 16:1278. [PubMed: 19355885]

6. Gupta AK, Naregalkar RR, Vaidya VD, Gupta M. Recent advances on surface engineering of magnetic iron oxide nanoparticles and their biomedical applications. Nanomedicine. 2007; 2:23–39. [PubMed: 17716188]
7. Corot C, Robert P, Idée JM, Port M. Recent advances in iron oxide nanocrystal technology for medical imaging. Adv Drug Deliv Rev. 2006; 58:1471–1504. [PubMed: 17116343]
8. Guthi JS, Yang SG, Huang G, Li S, Khemtong C, Kessinger CW, Peyton M, Minna JD, Brown KC, Gao J. MRI-visible micellar nanomedicine for targeted drug delivery to lung cancer cells. Mol Pharm. 7:32–40. [PubMed: 19708690]
9. Kumar A, Jena PK, Behera S, Lockey RF, Mohapatra S. Multifunctional magnetic nanoparticles for targeted delivery. Nanomedicine. 6:64–69. [PubMed: 19446653]
10. Yang L, Mao H, Wang YA, Cao Z, Peng X, Wang X, Duan H, Ni C, Yuan Q, Adams G, Smith MQ, Wood WC, Gao X, Nie S. Single chain epidermal growth factor receptor antibody conjugated nanoparticles for in vivo tumor targeting and imaging. Small. 2009; 5:235–243. [PubMed: 19089838]
11. Cho K, Wang X, Nie S, Chen ZG, Dong DM. Therapeutic Nanoparticles for Drug Delivery in Cancer. Clin Cancer Res. 2008; 14:131–1316.
12. Brannon-Peppas L, Blanchette JO. Nanoparticle and targeted systems for cancer therapy. Adv Drug Deliv Rev. 2004; 56:1649–1659. [PubMed: 15350294]
13. Li Y, Cozzi PJ. Targeting uPA/uPAR in prostate cancer. Cancer Treat Rev. 2007; 33:521–527. [PubMed: 17658220]
14. Ge Y, Elghetany MT. Urokinase plasminogen activator receptor (CD87): Something old, something new. Lab Hematol. 2003; 9:67–71. [PubMed: 12828301]
15. Pulukuri SM, Gondi CS, Lakka SS, Jutla A, Estes N, Gujrati M, Rao JS. RNA interference-directed knockdown of urokinase plasminogen activator and urokinase plasminogen activator receptor inhibits prostate cancer cell invasion, survival, and tumorigenicity in vivo. J Biol Chem. 2005; 280:36529–36540. [PubMed: 16127174]
16. Sheng S. The urokinase-type plasminogen activator system in prostate cancer metastasis. Cancer Metastasis Rev. 2001; 20(3–4):287–296. [PubMed: 12085967]
17. Hoyer-Hansen G, Ploug M, Behrendt N, Ronne E, Dano K. Cell-surface acceleration of urokinase-catalyzed receptor cleavage. Eur J Biochem. 1997; 243:21–26. [PubMed: 9030717]
18. Li H, Soria C, Griscelli F, Opolon P, Soria J, Yeh P, Legrand C, Vannier JP, Belin D, Perricaudet M, Lu H. Amino-terminal fragment of urokinase inhibits tumor cell invasion in vitro and in vivo: Respective contribution of the urokinase plasminogen activator receptor-dependent or -independent pathway. Hum Gene Ther. 2005; 16:1157–1167. [PubMed: 16218777]
19. Li Y, Cozzi PJ. Targeting uPA/uPAR in prostate cancer. Cancer Treat Rev. 2007; 33:521–527. [PubMed: 17658220]
20. Yang L, Mao H, Cao Z, Wang YA, Peng X, Wang X, Sajja HK, Wang L, Duan H, Ni C, Staley CA, Wood WC, Gao X, Nie S. Molecular imaging of pancreatic cancer in an animal model using targeted multifunctional nanoparticles. Gastroenterology. 2009; 136:1514–1525. [PubMed: 19208341]
21. Landen JW, Hau V, Wang M, Davis T, Ciliax B, Wainer BH, Van Meir EG, Glass JD, Joshi HC, Archer DR. Noscapine crosses the blood-brain barrier and inhibits glioblastoma growth. Clin Cancer Res. 2004; 10:5187–5201. [PubMed: 15297423]
22. Ke Y, Ye Y, Grossniklaus HE, Archer DA, Joshi HJ, Kapp JA. Noscapine inhibits tumor growth with little toxicity to normal tissues or inhibition of immune responses. Cancer Immunology, Immunotherapy. 2000; 49(4–5):217–225.
23. Ye K, Ke Y, Keshava N, Shanks J, Kapp JA, Tekmal RR, Petros J, Joshi HC. Opium alkaloid noscapine is an antitumor agent that arrests metaphase and induces apoptosis in dividing cells. Proc Natl Acad Sci U S A. 1998; 95:1601–1606. [PubMed: 9465062]
24. Sioka C, Kyritsis A. Central and peripheral nervous system toxicity of common chemotherapeutic agents. Cancer Chemotherapy and Pharmacology. 2009; 63:761–767. [PubMed: 19034447]
25. Perez EA. Microtubule inhibitors: Differentiating tubulin-inhibiting agents based on mechanisms of action, clinical activity, and resistance. Molecular Cancer Therapeutics. 2009; 8:2086–2095. [PubMed: 19671735]

26. Verstappen CCP, Heimans JJ, Hoekman K, Postma TJ. Neurotoxic complications of chemotherapy in patients with Cancer: clinical signs and optimal management. Drugs. 2003; 63:1549–1563. [PubMed: 12887262]
27. Park SB, Krishnan AV, Lin CS, Goldstein D, Friedlander M, Kiernan MC. Mechanisms underlying chemotherapy-induced neurotoxicity and the potential for neuroprotective strategies. Curr Med Chem. 2008; 15:3081–3084. [PubMed: 19075655]
28. Ke Y, Ye K, Grossniklaus HE, Archer DR, Joshi HC, Kapp JA. Noscapine inhibits tumor growth with little toxicity to normal tissues or inhibition of immune responses. Cancer Immunology Immunotherapy. 2000; 49:217–225.
29. Zhou J, Liu M, Aneja R, Chandra R, Joshi HC. Enhancement of paclitaxel-induced microtubule stabilization, mitotic arrest, and apoptosis by the microtubule-targeting agent EM012. Biochem Pharmacol. 2004; 68:2435–2441. [PubMed: 15548390]
30. Barken I, Geller J, Rogosnitzky M. Prophylactic noscapine therapy inhibits human prostate cancer progression and metastasis in a mouse model. Anticancer Res. 30:399–401. [PubMed: 20332445]
31. Jackson T, Chougule M, Ichite N, Patlolla R, Singh M. Antitumor activity of noscapine in human non-small cell lung cancer xenograft model. Cancer Chemotherapy and Pharmacology. 2008; 63:117–126. [PubMed: 18338172]
32. Bitoun E, Micheloni A, Lamant L, Bonnart C, Tartaglia-Polcini A, Cobbold C, Al Saati T, Mariotti F, Mazereeuw-Hautier J, Boralevi F, Hohl D, Harper J, Bodemer C, D'Alessio M, Hovnanian A. LEKTI proteolytic processing in human primary keratinocytes, tissue distribution and defective expression in Netherton syndrome. Hum Mol Genet. 2003; 12:2417–2430. [PubMed: 12915442]
33. Dahlstrom B, Mellstrand T, Lofdahl CG, Johansson M. Pharmacokinetic properties of noscapine. Eur J Clin Pharmacol. 1982; 22:535–539. [PubMed: 7128665]
34. Karlsson MO, Dahlstrom B, Eckernas SA, Johansson M, Alm AT. Pharmacokinetics of oral noscapine. Eur J Pharm Biopharm. 1990; 39:275–279.
35. Ye K, Ke Y, Keshava N, Shanks J, Kapp JA, Tekmal RR, Petros J, Joshi HC. Opium alkaloid noscapine is an antitumor agent that arrests metaphase and induces apoptosis in dividing cells. Proc Natl Acad Sci USA. 1998; 95:1601–1606. [PubMed: 9465062]
36. Gaumet M, Vargas A, Gurny R, Delie F. Nanoparticles for drug delivery: The need for precision in reporting particle size parameters. Eur J Pharm Biopharm. 2008; 69:1–9. [PubMed: 17826969]
37. Veiseh O, Gunn JW, Zhang M. Design and fabrication of magnetic nanoparticles for targeted drug delivery and imaging. Advanced Drug Delivery Reviews. 2010; 62:284–304. [PubMed: 19909778]
38. Cho K, Wang X, Nie S, Chen ZG, Shin DM. Therapeutic nanoparticles for drug delivery in cancer. Clin Cancer Res. 2008; 14:1310–1316. [PubMed: 18316549]
39. Gupta AK, Wells S. Surface-modified superparamagnetic nanoparticles for drug delivery: preparation, characterization, and cytotoxicity studies. IEEE Trans Nanobioscience. 2004; 3:66–73. [PubMed: 15382647]
40. Zavisova V, Koneracka M, Strbak O, Tomasovicova N, Kopcansky P, Timko M, Vavra I. Encapsulation of indomethacin in magnetic biodegradable polymer nanoparticles. J Magn Magn Mater. 2007; 311:379–382.
41. Yang L, Cao Z, Sajja HK, Mao H, Wang L, Geng H, Xu H, Jiang T, Wood WC, Nie SWY. Development of receptor targeted magnetic iron oxide nanoparticles for efficient drug delivery and tumor Iimaging. J Biomed Nanotech. 2008; 4:1–11.
42. Rajvir D, Hae Duck P, John C, Robert LV, George F, Perinchery N. Inhibition of tumorigenic potential and prostate-specific antigen expression in LNCaP human prostate cancer cell line by 13-*cis*-retinoic acid. Int J Cancer. 1994; 59:126–132. [PubMed: 7523313]
43. Laniado ME, Lalani EN, Fraser SP, Grimes JA, Bhangal G, Djamgoz MB, Abel PD. Expression and functional analysis of voltage-activated Na+ channels in human prostate cancer cell lines and their contribution to invasion in vitro. Am J Pathol. 1997; 150:1213–1221. [PubMed: 9094978]

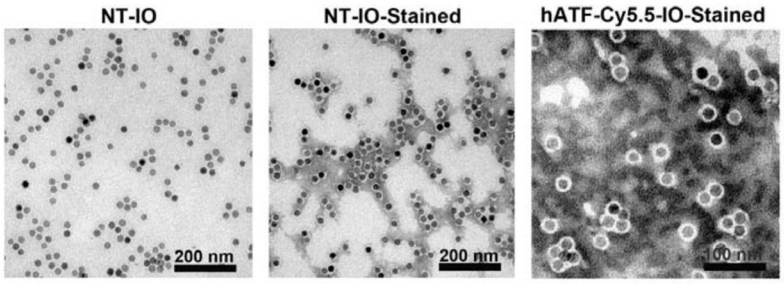

Fig. 1.

TEM micrographs of polymer coated IO NPs before and after conjugation of peptide-dye conjugates. *Left*, NT-IO (Bar=200 nm). *Middle*, NT-IO-Stained: negative stained IO NPs showed the polymer layer surrounding the IO core (Bar=200 nm). *Right*, hATF-Cy5.5-IO-Stained: negative-stained polymer coated IO NPs after conjugation of peptide-dye showed roughness on the edge of polymer coating thus limiting exact NP size determination even at higher magnification (Bar= 100 nm).

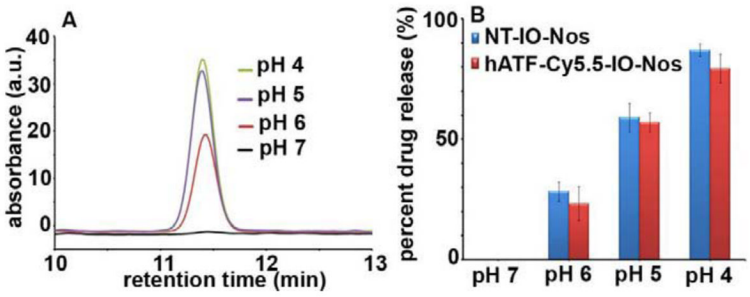

Fig. 2.

Examination of pH-dependent release of Nos from targeted and non-targeted NPs. 10 μL of NT-IO-Nos or hATF-Cy5.5-IO-Nos NPs were placed in different buffer solutions with pH 4, 5, 6 and 7 for 2h at 37°C. ***A***, Overlay of HPLC chromatograms illustrate the amount of Nos released from hATF-Cy5.5-IO-Nos NPs in buffers with different pHs. While no pronounced peak was detected for Nos at pH 7, a Nos peak was detected and increased in size at lower pHs. ***B***, Percentage of drug released from NT-IO-Nos and hATF-Cy5.5-IO-Nos NPs calculated from the area under the peak of the HPLC chromatograms.

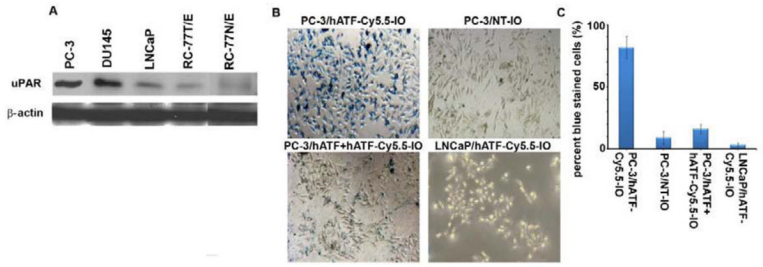

Fig. 3.

A, uPAR expression was examined by immunoblotting of whole cell lysates from PC-3, DU145, LNCaP, and RC-77T/E. β-actin was used as a loading control. ***B***, Prussian blue staining of PC-3 cells treated with 30 pmole of NT-IO, hATF-Cy5.5-IO NPs, free hATF peptide (10 times excess as a competition probe to occupy existing receptors) followed by hATF-Cy5.5-IO NPs. ***C***, Quantitation of PC-3 cells stained with Prussian blue.

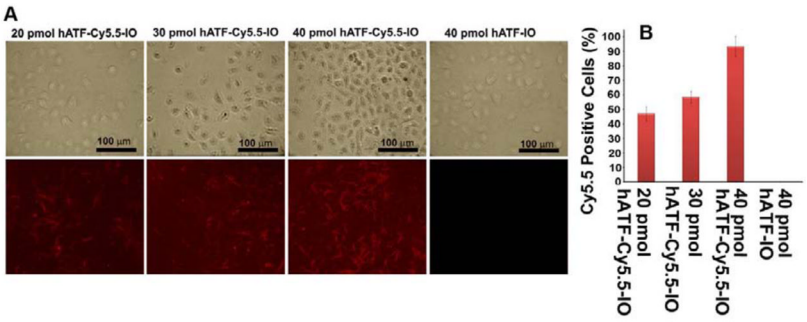

Fig. 4.

Binding specificity of hATF-Cy5.5-IO NPs to PC-3 cells using *in vitro* NIR optical imaging. ***A***, DIC and NIR images of PC-3 cells treated with 20, 30, and 40 pmoles/mL of hATF-Cy5.5-IO-Nos NPs. PC-3 cells treated with hATF-IO NPs served as a negative control. (Scale bar=100 μm) ***B***, Quantitation of Cy5.5-positive cells in 20, 30, 40 pmole hATF-Cy5.5-IO.

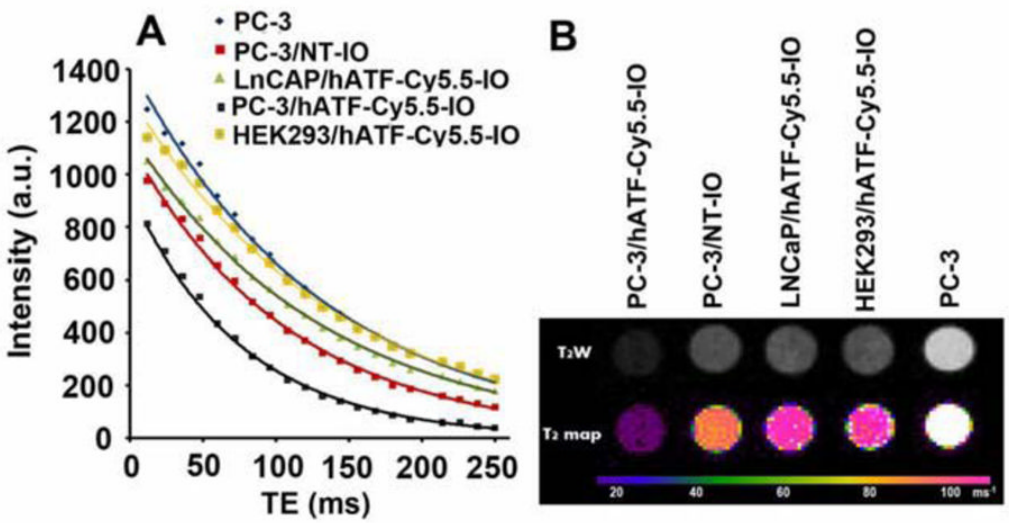

Fig. 5.

In vitro MRI scans show binding specificity and negative enhancement effect on T2-weighted images by NT-IO and hATF-Cy5.5-IO NPs on PC-3 cells. ***A***, Reduction in T2 relaxation time in treated cells ***B***, T2W and T2 maps correlated with reduction in T2 values.

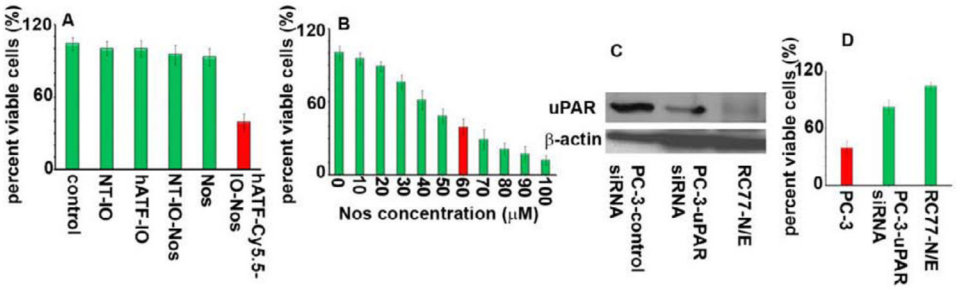

Fig 6.

Cytotoxicity assay to test the efficiency of hATF-mediated Nos delivery into PC-3 cells. ***A***, hATF-Cy5.5-IO-Nos NPs decreased the percentage of viable cells (~60%) compared to free Nos or NT-IO-Nos. Cell viability remained same with NT-IO and hATF-IO NPs. ***B***, Percent cell viability in PC-3 cells treated with 0–100 μM free Nos. ***C,*** Immunoblot analysis of uPAR expression in PC-3 cells transfected with control or uPAR siRNA. RC77-N/E expressed very low uPAR protein. ***D***, Bar graph showing cell death in PC-3 or RC-77N/E cells transfected with control or uPAR siRNA in combination with hATF-Cy5.5-IO-Nos NPs.

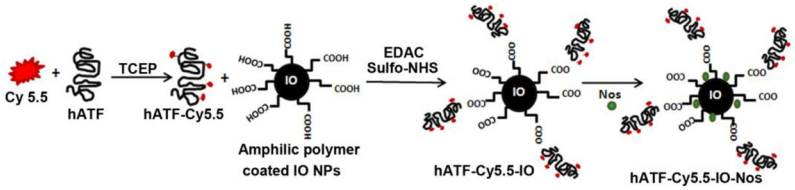

Scheme 1.

Schematic of preparation steps of uPAR-targeted hATF-Cy5.5-IO-Nos NPs. The Cy5.5 dye was conjugated to cysteine residues of hATF peptide. The hATF-Cy5.5 complex was then conjugated to the carboxylic ends of the amphiphilic polymer coated IO NPs (10 nm in diameter) followed by Nos loading by physical adsorption onto the amphiphilic polymer coating.

Table 1

Size and zeta potential characterization of NT-IO, hATF-Cy5.5-IO, and hATF-Cy5.5-IO-Nos NPs

Nanoparticles	Size (nm)		Zeta Potential (mV)
	TEM	DLS	
NT-IO	14.4 ± 2.1	21.36 ± 1.6	−52.41 ± 3.1
hATF-Cy5.5-IO	------	35.21± 3.7	−33.4 ± 5.61
hATF-Cy5.5-IO-Nos	------	35.62 ± 4.1	−21.6 ± 3.3

Table 2

Encapsulation efficiency of Nos in NT-IO and hATF-Cy5.5-IO NPs.

Nanoparticles	NT-IO-Nos	hATF-Cy5.5-IO-Nos
% Encapsulated drug	98.7 ± 0.7	88.2 ± 2.3
Number of Nos molecules per	740 ± 98	558 ± 74